Journal of Materials Chemistry A

ROYAL SOCIETY OF CHEMISTRY

PAPER

View Article Online
View Journal | View Issue

Cite this: J. Mater. Chem. A, 2025, 13, 17054

Small voltage hysteresis and flat plateaus in Ca-metal batteries using a Ti-based NASICON cathode†

Kohei Shibuya,[ab] Kazuaki Kisu,[*c] Takara Shinohara,[ab] Kosuke Ishibashi,[d] Hiroshi Yabu[d] and Shin-ichi Orimo[*ad]

Ca-metal batteries have emerged as promising candidates for post-Li-ion batteries owing to their high energy density, cost-effectiveness, and natural abundance. However, few cathode materials have been evaluated for full-cell configurations with Ca-metal anodes, and most of these materials exhibit large voltage hysteresis and sloping voltage profiles. In this study, we propose polyanionic Na superionic conduction (NASICON)-type $NaTi_2(PO_4)_3$ (NTP) as a cathode material for Ca-metal batteries, leveraging its relatively large lattice size among NASICON compounds to accelerate Ca^{2+} diffusion. Nanoparticulate NTP/carbon nanotube (CNT) composites were synthesised *via* solvothermal synthesis. The composite structure consisted of NTP nanoparticles uniformly dispersed within a conductive CNT network, which provided high electronic conductivity and short Ca^{2+} diffusion pathways, enabling fast electrochemical reactions. By combining NTP cathodes with a Ca-metal anode and a hydride-based electrolyte, *i.e.* $Ca(CB_{11}H_{12})_2$ in 1,2-dimethoxyethane/tetrahydrofuran, capable of supporting reversible Ca plating/stripping at room temperature, we fabricated Ca-metal batteries that achieved a reversible Ca storage capacity of 40.6 mA h g^{-1} at 5 mA g^{-1}. Notably, these cells exhibited small voltage hysteresis and flat voltage profiles, indicating rapid Ca^{2+} diffusion. *Ex situ* analysis, including X-ray diffraction and X-ray photoelectron spectroscopy, confirmed the reversible insertion and extraction of Ca^{2+} within the NTP framework. This study provides valuable insights into the design of practical Ca cathodes with enhanced ion-transport properties, paving the way for the development of high-performance Ca-metal batteries.

Received 31st January 2025
Accepted 23rd April 2025

DOI: 10.1039/d5ta00829h

rsc.li/materials-a

Introduction

The rapidly growing market for electric vehicles and grid energy storage has generated strong demand for energy-storage systems with higher energy densities and lower costs than current Li-ion batteries (LIBs).[1,2] Ca-metal batteries have attracted significant attention due to the high volumetric capacity (2072 mA h cm^{-3}) and low reduction potential (−2.87 V *vs.* SHE) of Ca metal.[3–5] Moreover, Ca is the fifth-most abundant element in the Earth's crust and its salts are generally nontoxic, leading to low costs and high safety.[6,7] However, despite these advantages, the practical realisation of Ca-metal batteries remains hindered by the absence of a well-defined model cathode material that enables reversible Ca^{2+} storage in full-cell configurations.

A model cathode plays a critical role in the advancement of battery technology, as exemplified by Mo_6S_8 in Mg-ion batteries, which has served as a benchmark for understanding Mg^{2+} insertion/extraction.[8–10] To serve as an effective model cathode for Ca-metal batteries, a material must meet several key criteria, including a simple reaction mechanism, a flat voltage plateau, low hysteresis, high structural stability, and an appropriate operating voltage. However, no reported Ca-metal battery cathode meets these requirements, presenting a major obstacle to further research and development.

Research on cathodes using full-cell configurations remains in its early stages due to the limited availability of electrolytes compatible with Ca plating/stripping, restricting cathode evaluations primarily to half-cell studies with activated-carbon electrodes as substitutes for Ca metal. While half-cell measurements provide insight into intrinsic properties of cathode materials,[11–17] they do not fully capture the electrochemical complexities of practical full-cell operation. Consequently, many materials that exhibit reversible Ca^{2+} insertion/extraction in half-cells demonstrate poor or non-reversible

[a]Institute for Materials Research (IMR), Tohoku University, Katahira 2-1-1, Aoba-ku, Sendai 980-8577, Japan
[b]Ichikawa Research Centre, Sumitomo Metal Mining Co. Ltd., Nakakokubun 3-18-5, Ichikawa, Chiba 272-8588, Japan
[c]College of Engineering, Shibaura Institute of Technology, Toyosu 3-7-5 Koto-ku, Tokyo 135-8548, Japan. E-mail: kkisu@shibaura-it.ac.jp
[d]Advanced Institute for Materials Research (AIMR), Tohoku University, Katahira 2-1-1, Aoba-ku, Sendai 980-8577, Japan. E-mail: shin-ichi.orimo.a6@tohoku.ac.jp

† Electronic supplementary information (ESI) available. See DOI: https://doi.org/10.1039/d5ta00829h

performance in full-cell tests,[18–20] underscoring the necessity of full-cell evaluations.

Recent advancements in electrolytes such as $Ca(BH_4)_2$,[21,22] $Ca[B(hfip)_4]_2$,[23,24] and $Ca(CB_{11}H_{12})_2$ (ref. 25 and 26) have enabled full-cell testing, shifting research beyond half-cell screening. Various candidates, including sulfides (Sulfur (S),[27,28] CuS,[29,30] and VS_4 (ref. 31)), Se,[32] C-based materials (graphite[33] and free-standing lattice-expanded graphitic carbon fiber (FLEGCF)[34]), organic compounds (1,4-polyanthraquinone (14PAQ),[35] poly(-anthraquinonyl sulfide) (PAQS),[36] polytriphenylamine/graphene nanoplates (PTGNP),[37] and 3,4,9,10-perylenetetracarboxylic dianhydride (PTCDA)[38]), metal oxides ($CaV_6O_{16}\cdot 2.8H_2O$ (CVO)[18]), and fluorophosphates ($NaV_2PO_{4.8}F_{0.7}$,[19] $NaV_2(PO_4)_2F_3$,[20], (NVPF) and K_xVPO_4F ($x \sim 0$) (K_0VPF)[39]) have been explored. However, each of these materials faces fundamental limitations. Sulfides suffer from low cycling efficiency due to conversion-type reactions. Se undergoes dissolution and pulverisation, leading to rapid capacity fade. Carbon-based materials either operate at low voltages (*e.g.*, graphite) or suffer from high polarisation shifts (*e.g.*, FLEGCF). Organic compounds, while offering good cycling stability, dissolve in electrolytes, causing performance degradation. Fluorophosphates, despite their high voltage operation, exhibit large voltage hysteresis and sloping voltage profiles, which reduce energy efficiency. Given these limitations, the lack of a model cathode remains a critical bottleneck in the field.

Among polyanionic compounds, NASICON-type materials have gained attention due to their three-dimensional interconnected channels, which enhance Ca^{2+} mobility. While fluorophosphates offer the advantage of high voltage,[40] NASICON-type polyanionic compounds have higher ionic conductivity.[41] $NaV_2(PO_4)_3$ (NVP) has been extensively investigated as a potential cathode for Ca-ion batteries due to its structural stability and ability to accommodate multivalent ions. NVP has demonstrated reversible Ca^{2+} insertion/extraction in half-cells, confirming the viability of NASICON-type frameworks for Ca^{2+} storage. However, in full-cell configurations, NVP exhibits substantial voltage hysteresis and a sloping voltage profile, indicating significant kinetic limitations in Ca^{2+} mobility. This suggests that while the NASICON framework itself is promising, improving ion diffusion within the structure is critical for practical application.

Building upon this insight, we propose $NaTi_2(PO_4)_3$ (NTP) as an improved NASICON-type cathode for Ca-metal batteries. Compared to NVP, NTP features a larger lattice size, which provides superior rate performance in Na-ion batteries[42] and is expected to enhance Ca^{2+} diffusivity, thereby mitigating the kinetic limitations observed in NVP. This fast-ion diffusion property can enable flatter voltage profiles and reduce voltage hysteresis. Furthermore, NTP offers a moderate average working voltage compared to NVP (NTP: 2.1 V *vs.* Na^+/Na, NVP: 3.4 V *vs.* Na^+/Na),[42] which may contribute to reduce electrolyte decomposition. These advantages position NTP as a strong candidate for a model cathode. However, despite these advantages, NTP has only been reported as a Na^+ host,[43–45] and its feasibility for Ca^{2+} storage remains unexplored.

In this study, the electrochemical properties of NTP as a Ca^{2+} host material were investigated using a Ca full-cell configuration consisting of a Ca-metal anode and a hydride-based electrolyte ($Ca(CB_{11}H_{12})_2$ in DME/THF), which exhibits high compatibility with Ca metal and minimises the impact of electrolyte–Ca metal interactions in this system. This study provides the first demonstration of reversible Ca^{2+} insertion/extraction in NTP, exhibiting minimal voltage hysteresis and a flat voltage plateau, both of which are key characteristics for a practical model cathode. The galvanostatic intermittent titration technique (GITT) test revealed that the fast Ca^{2+} diffusion rate in NTP is comparable to the Li^+ diffusion rate in conventional cathodes for Li-ion batteries. *Ex situ* X-ray diffraction (XRD) and X-ray photoelectron spectroscopy (XPS) analyses, conducted before and after discharge and charge, confirmed the reversible structural changes in NTP and the corresponding valence state of Ti. These findings highlight the potential of NTP as a model cathode material for Ca-metal batteries, offering small voltage hysteresis and a single voltage plateau enabled by fast Ca^{2+} diffusion.

Methods

Air-sensitive materials were prepared and handled under a dry Ar atmosphere using a glovebox and Schlenk techniques.

Materials

CH_3COONa (Sigma-Aldrich, ≥99.0%), $Ti[O(CH_2)_3CH_3]_4$ (Sigma-Aldrich, ≥99.0%), and H_3PO_4 (Sigma-Aldrich, crystalline, ≥99.999% trace metals basis) or $NH_4H_2PO_4$ (Sigma-Aldrich, Bioultra, ≥99.5% (T)) were used as sources of Na, Ti, and P, respectively, while citric acid (Kanto Chemical Co., Inc.) was employed to assist the solvothermal process with a chelating effect in the synthesis of NTP. Multi-walled carbon nanotubes (CNTs, Sigma-Aldrich, >98% carbon basis, outer diameter (O.D.) × *L* 6–13 nm × 2.5–20 μm) were selected as the carbon matrix. Ultrapure water (FUJIFILM Wako Pure Chemical Co., Ltd.) and superdehydrated ethanol (FUJIFILM Wako Pure Chemical Co., Ltd.) were used as solvents. $CsCB_{11}H_{12}$ (Katchem Ltd.) and $CaCO_3$ (FUJIFILM Wako Pure Chemical Co., Ltd.) were used to prepare the $Ca(CB_{11}H_{12})_2$ salt, and Amberlite IR120B (DuPont Water Solutions) was used for ion exchange. DME (Sigma-Aldrich) and THF (Sigma-Aldrich) were used as received. NaTFSI (Sigma-Aldrich) was used as the electrolyte salt in the Na half-cell.

Synthesis of NTP

NTP with two distinct particle sizes was synthesised using a solvothermal method, resulting in a nanoparticulate NTP/CNT composite (ncNTP) and a larger-particle NTP (lpNTP). Two solutions—labelled Solutions A and B—were prepared with specific reagents tailored to each particle type. Solution A was made by dissolving 0.1016 g of CH_3COONa, 0.364 g of H_3PO_4 (or 0.428 g of $NH_4H_2PO_4$ for lpNTP synthesis), and 0.238 g of citric acid in either 12 mL of superdehydrated ethanol with 0.5 mL of ultrapure water (for ncNTP) or 12.5 mL of ultrapure water (for

lpNTP). Solution B consisted of 0.843 g of $Ti[O(CH_2)_3CH_3]_4$ dissolved in 1.25 mL of superdehydrated ethanol. To synthesise ncNTP, 0.2142 g of CNTs was added to Solution A, calculated to achieve a final composition of NTP 80 wt% and CNTs 20 wt%, whereas no CNTs were used for synthesising lpNTP. Solution A (with and without CNTs) was stirred vigorously at 700 rpm at room temperature using a magnetic stirrer. Solution B was then added dropwise to Solution A with continuous stirring for 30 min. The resulting mixture was transferred to a 25-mL Teflon-lined stainless-steel high-pressure reaction vessel, sealed, and heated at 180 °C for 12 h. After cooling to room temperature, the suspension was filtered, washed multiple times with water and ethanol, and dried under vacuum at 80 °C for 12 h. A final heat treatment in an Ar atmosphere at 750 °C for 4 h yielded the ncNTP or lpNTP products.

Characterisation of ncNTP and lpNTP

The synthesised samples were characterised *via* X-ray diffractometry using an X'Pert Pro diffractometer (PANalytical) with Cu Kα radiation (wavelength $\lambda = 1.5406$ Å for Kα1 and 1.5444 Å for Kα2). The morphology was examined *via* field-emission scanning electron microscopy (FE-SEM, JSM-7800F, JEOL) and energy-dispersive X-ray spectroscopy (EDS). The microstructure of ncNTP was examined using transmission electron microscopy (TEM, H-7650, Hitachi High-Technologies). The samples were prepared by casting a dispersion of ncNTP in ethanol onto a grid. The valence state of Ti was assessed using XPS (PHI 5000 VersaProbe II, ULVAC PHI, Inc). All samples were sealed in airtight sample holders to avoid exposure to ambient conditions during sample transfer.

Synthesis of $Ca(CB_{11}H_{12})_2$ in DME/THF electrolytes

The synthesis of $Ca(CB_{11}H_{12})_2$ in DME/THF electrolytes was described in our previous work. For details regarding the synthesis procedure, please refer to the referenced paper.[46]

Electrochemical analyses and battery tests

The ncNTP and lpNTP electrodes were prepared by mixing 78 wt% of the composite, 12 wt% styrene-butadiene rubber, 6 wt% carboxymethyl cellulose, and 4 wt% single-walled carbon nanotubes in a water/ethanol mixture. The resulting slurry was uniformly coated onto etched Al foil, which served as the current collector, and dried under vacuum at 80 °C for 12 h. The active material loading of the electrodes was 1.21 mg cm^{-2} for ncNTP and 1.16 mg cm^{-2} for lpNTP, calculated based on the electrode mass, area, intended active material content, and the composition of NTP and CNTs in both ncNTP and lpNTP.

For the battery tests, the electrodes were assembled with a separator, electrolyte, and a Ca-metal anode in a stainless-steel electrochemical-cell holder. The tests were performed at a current density of 5 mA g^{-1} at 25 °C within the voltage range of 1.6–2.5 V using a battery test system (580 Battery Test System, Scribner Associates, Inc). To verify NTP's capability as a Na^+ host and to elucidate the specific advantages and challenges of Ca insertion/extraction, Na half-cells were fabricated using activated carbon instead of the Ca-metal anode and NaTFSI in DME as the electrolyte. The electrochemical evaluation of the Na half-cell was conducted at 10 times the rate of the Ca cell.

Cyclic voltammetry (CV) and electrochemical impedance spectroscopy (EIS) were performed using a multichannel potentiostat (1470E Cell Test System, Solartron Analytical) and a multichannel parallel impedance analyser (1455A, Solartron Analytical). CV was conducted at a scan rate of 0.1 mV s^{-1} over a voltage range of 1.5–2.6 V *vs.* Ca^{2+}/Ca. The impedance spectra were recorded by applying an alternating-current (AC) voltage of 5 mV over a frequency range of 1 MHz to 10 mHz. The GITT test was performed using a galvanostat (SP-200, Biologic). During the GITT, the battery cell was charged at a current density of 5 mA g^{-1} for 30 min, followed by an open-circuit rest period of 10 min.

Results and discussion

Characterisation of ncNTP and lpNTP

The crystal structure of NTP is based on a rhombohedral NASICON-type framework (space group: $R\bar{3}c$), as illustrated in Fig. 1a. NTP is built from isolated TiO_6 octahedra and PO_4 tetrahedra interlinked by corner sharing, which is analogous to the structure of NVP, in which V replaces Ti. XRD patterns for the synthesised ncNTP, identified as NASICON-structured NTP, confirm that ncNTP adopts the same structure, with lattice constants of $a = 8.4828(2)$ Å and $c = 21.7760(8)$ Å (Fig. 1b and Table S1†). The broad peak observed at approximately 25° in the XRD pattern suggests the presence of CNTs. Similarly, the XRD profile of lpNTP exhibits peaks corresponding to both NTP and rutile TiO_2, indicating that NTP is the predominant phase, whereas TiO_2 exists as a minor secondary phase (Fig. S1†).

SEM observations of ncNTP revealed NTP nanoparticles embedded within the CNT matrices, which were used to analyse the morphology of the composite (Fig. 1c). The EDS spectrum confirmed the presence of key elements in NTP, exhibiting signals corresponding to Na at 1.04 keV (Na Kα), P at 2.01 keV (P Kα), and Ti at 4.51 keV (Ti Kα) and 4.93 keV (Ti Kβ) (Fig. S2†). In addition, an Al signal at 1.48 keV originating from the sample stage was detected. EDS mapping revealed a uniform distribution of all elements constituting NTP throughout the CNT at the micron scale. In contrast, an SEM image of lpNTP revealed a larger, chunk-like NTP particle exceeding 20 μm in size. EDS mapping confirmed the uniform distribution of all NTP elements in the particles (Fig. S3†).

To investigate the nanoscale structure and particle size of ncNTP, TEM analysis was conducted (Fig. 1d). The observed black particles were identified as NTP nanoparticles, with sizes ranging from approximately 10 to 50 nm. The fibrous structures visible in the TEM images were attributed to CNTs. TEM observations confirmed that NTP nanoparticles are embedded within the CNT matrix. This entanglement and dispersion of NTP nanoparticles within the CNT matrix suggest the establishment of efficient electron conduction pathways and a short diffusion length of Ca^{2+} in NTP crystals (Fig. 1e). While a well-dispersed NTP/CNT composite was achieved, aggregation of NTP particles was also observed, which may hinder

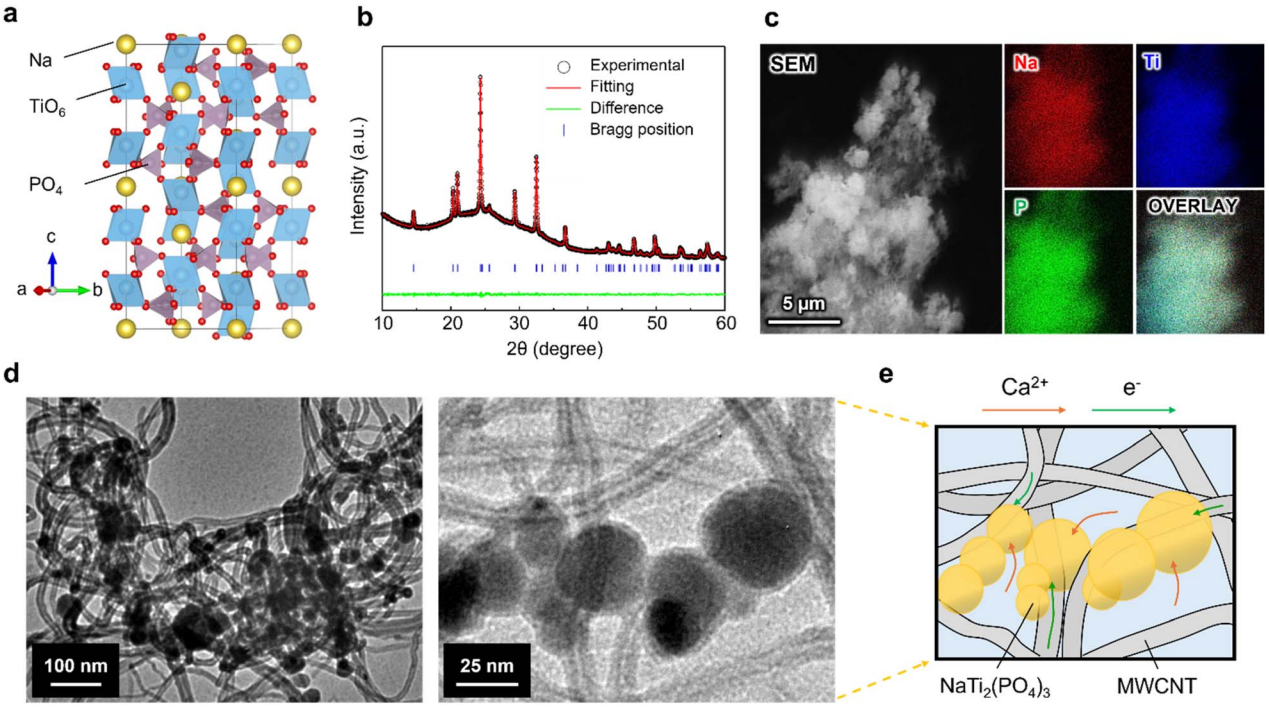

Fig. 1 Structural characterisation of the nanoparticulate NTP/CNT composite (ncNTP). (a) Crystal structure of NTP. (b) Rietveld refinement of ncNTP. (c) SEM image of ncNTP along with EDS maps for Na, Ti, and P. (d) TEM images of ncNTP. (e) Schematic of Ca^{2+} and electron paths of ncNTP.

electrochemical performance owing to insufficient contact with the CNT matrix (Fig. S4†).

Ca-storage-based electrochemical performance

The Ca-storage-based electrochemical performance of ncNTP was evaluated in a full-cell configuration using Ca metal as both the counter and reference electrodes, with the hydride-based electrolyte $Ca(CB_{11}H_{12})_2$ in DME/THF (Fig. 2a). CV measurements were performed to investigate the insertion and extraction of Ca^{2+}. In the initial anodic scan, a reduction peak at 1.75 V was clearly observed (Fig. 2b), indicating the insertion of Ca^{2+} into the ncNTP electrode. During the initial cathodic scan, a sharp oxidation peak was observed at 2.05 V, corresponding to the extraction of Ca^{2+}. Compared with previous studies on test cells using a Ca-metal anode, in which broader peaks were observed,[30,33] we observed a relatively sharp peak indicating a low overvoltage. This was likely due to fast Ca^{2+} diffusion in NTP. Previous reports have suggested that the average reaction voltage of $CaTi_2(PO_4)_3$ is 1.6 V according to calculations,[47] but the obtained average voltage of 1.9 V is slightly higher. This difference was likely due to the varying inductive effects of Na^+ and Ca^{2+} in the framework. During the 2nd and 3rd cycles, the reduction-peak intensity decreased and shifted to lower voltages, suggesting an increase in overvoltage (Fig. S5†). This is attributed to electrolyte decomposition. Another possible factor is the structural changes in the NTP framework caused by Ca^{2+} insertion. The intensity of the oxidation peak also decreased, but its position remained unchanged, indicating that the activation energy of the oxidation was largely unaffected. The temperature dependence of ncNTP is presented in Fig. S6.† Although the charge capacity exhibited minimal variation with increasing temperature, the discharge capacity showed an increase, suggesting an enhancement of side reactions. Compared with the insertion/extraction of Na^+, broader peaks were observed during the reaction with Ca^{2+}, implying slower kinetics for the insertion/extraction of Ca^{2+} and more pronounced structural changes in NTP upon Ca^{2+} insertion (Fig. S7†).

The galvanostatic discharge and charge performance of ncNTP (Fig. 2c) was evaluated within the voltage range of 1.5–2.6 V at a current density of 5 mA g^{-1} and room temperature. The theoretical capacity of a two-electron reaction involving one Ca^{2+} insertion per formula unit of NTP is 132.8 mA h g^{-1}. The initial discharge and charge capacities are 53.4 and 40.6 mA h g^{-1}, corresponding to 0.40 and 0.30 mol of Ca^{2+} per 1 mol of NTP, respectively. These values fall short of the theoretical capacity, suggesting that the relatively large NTP particles impede the full progression of the reaction. Furthermore, lpNTP failed to function in a Ca full-cell, likely because of the large particles (Fig. 2c inset). In contrast, both ncNTP and lpNTP exhibited good performance in the Na half-cell (Fig. S8 and S9†). This discrepancy is attributed to three factors. (1) The diffusion coefficient of Ca^{2+} ($D_{Ca^{2+}}$) is lower than that of Na^+ (D_{Na^+}). (2) Higher reaction energy for Ca^{2+} insertion/extraction than that for Na^+, indicated by a lower average reaction voltage (Ca: 1.7 V *vs.* Na^+/Na, Na: 2.1 V *vs.* Na^+/Na, Fig. S10†). (3) The significant changes in the crystal structure induced by Ca^{2+} insertion may lead to material degradation (discussed in detail

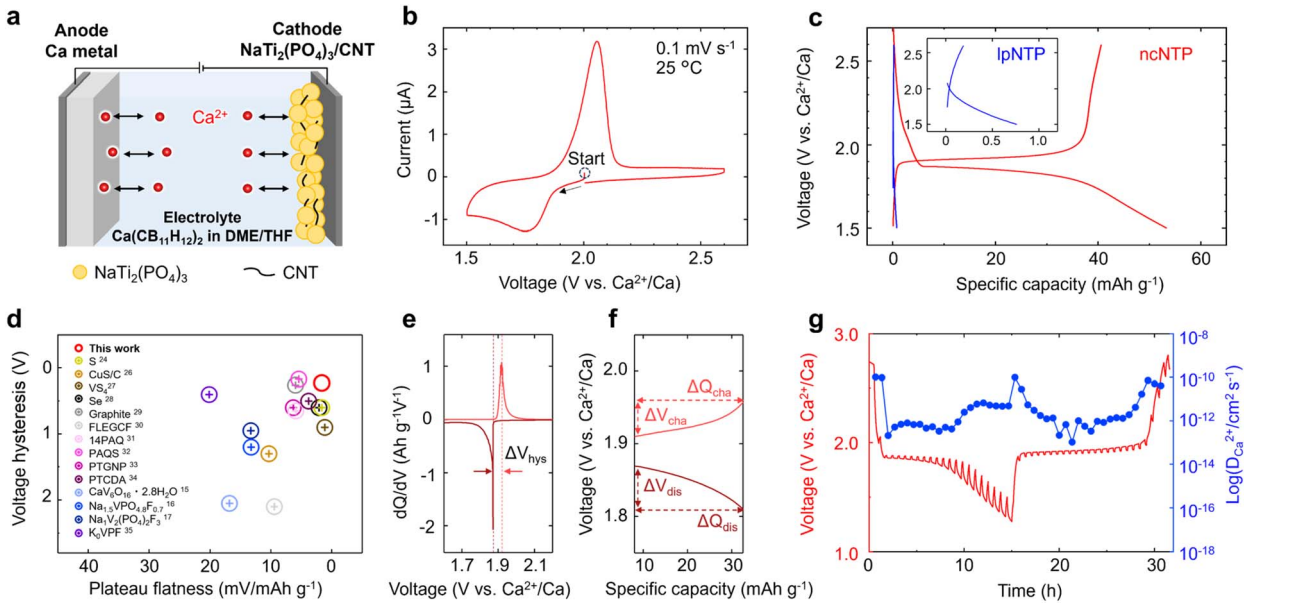

Fig. 2 Ca-storage performance of NTP. (a) Schematic of a prototype Ca-metal battery, consisting of an NTP/CNT composite cathode, a Ca-metal anode, and a hydride-based electrolyte, *i.e.* $Ca(CB_{11}H_{12})$ in DME/THF. (b) CV curve of ncNTP for the 1st cycle obtained at a scan rate of 0.1 mV s^{-1} in the voltage range of 1.5–2.6 V *vs.* Ca^{2+}/Ca. (c) Voltage profile of ncNTP during the 1st cycle acquired at a current density of 5 mA g^{-1} in the voltage range of 1.5–2.6 V at room temperature (25 °C). The inset shows the voltage profile of lpNTP. (d) Voltage hysteresis and plateau flatness of previously reported Ca-metal batteries. (e) dQ/dV curve of ncNTP for the 1st cycle. (f) Voltage profile of ncNTP during the 1st cycle in the SOC 20–80% area. (g) GITT test of lpNTP during the 1st cycle at a rate of 5 mA g^{-1}.

in the following section). These Na half-cell evaluations are validated through comparison with full-cell evaluations (Fig. S11†).

To further assess the electrochemical performance of ncNTP, galvanostatic charge and discharge measurements were conducted at various current densities (Fig. S12†). At moderate rates (10 and 20 mA g^{-1}), a distinct plateau was observed, suggesting that ncNTP exhibits relatively high Ca^{2+} diffusivity, enabling Ca^{2+} insertion and extraction even at elevated rates. However, as the rate increased, a progressive capacity fade was observed, which can be attributed to the expansion of unreacted regions within the electrode. Several factors may contribute to this phenomenon: (i) structural distortions and phase transitions – the insertion of Ca^{2+} induces structural strain and phase transitions, leading to localised increases in diffusion barriers that hinder further ion transport. (ii) Delayed Ca^{2+} supply from the electrolyte – since Ca^{2+} is divalent and exhibits a larger solvation structure than monovalent cations, its desolvation and transport kinetics are inherently sluggish. This limitation becomes more pronounced at high rates, exacerbating the capacity fade. Additionally, a notable increase in overpotential was observed during discharge compared to charge, suggesting that Ca^{2+} insertion is kinetically more hindered than its extraction. This asymmetry implies that additional energy is required to overcome the barriers associated with Ca^{2+} intercalation, likely due to stronger electrostatic interactions and steric hindrances within the host framework. These findings highlight the favorable Ca^{2+} diffusion properties of ncNTP at moderate rates while also revealing the kinetic limitations that arise at higher current densities, providing insight into the rate-limiting factors in Ca-ion storage using NTP.

The voltage profile of the full-cell using ncNTP and Ca metal, as shown in Fig. 2c, exhibited small voltage hysteresis and a non-sloping curve. To evaluate this characteristic quantitatively, calculations were performed as described below, and the results were compared with previous reports on cathodes for Ca-metal batteries (Fig. 2d). Voltage hysteresis (V_{hys}) is defined as the voltage difference between the peak tops of the charge and discharge voltages in the dQ/dV curves. The dQ/dV profile of ncNTP exhibited redox peaks with maxima at 1.87 and 1.91 V, corresponding to a hysteresis of only 0.04 V (Fig. 2e). These values were obtained using a three-electrode configuration. Considering the potential of the counter electrode during discharge (0.01 V) and charge (−0.18 V), the discharge and charge voltages in a two-electrode configuration were estimated to be 1.86 and 2.09 V, respectively, corresponding to a hysteresis of 0.23 V. If the dQ/dV curve is not presented in the paper, V_{hys} is defined as the difference between the charge and discharge voltages at a state of charge (SOC) of 50%. The plateau flatness was defined as the average of the discharge and charge flatness, which was calculated as the voltage change (V_{dis} and V_{cha}) divided by the capacity change (Q_{dis} and Q_{cha}) within the plateau region from 20% to 80% SOC (Fig. 2f). As shown in Fig. 2d, Ca-metal batteries using ncNTP exhibited smaller voltage hysteresis and flatter plateaus than previously reported cathodes for Ca-metal batteries.

To investigate the Ca^{2+} diffusion kinetics in ncNTP, the GITT test was performed, and the Ca^{2+} diffusion coefficient ($D_{Ca^{2+}}$) was calculated (Fig. 2g). During discharge, two distinct regions

were observed: a plateau in the first half of the curve and a broad region in the second half. These regions are also reflected in the $D_{Ca^{2+}}$ profile, suggesting that the Ca^{2+} diffusion pathway changes with the discharge reaction mechanism. In contrast, during charging, a single region was observed in both the GITT and $D_{Ca^{2+}}$ profiles. The average $D_{Ca^{2+}}$ values during discharge and charge in the plateau region (discharge: SOC 20–60%, charge: SOC 20–80%) were calculated to be 5.7×10^{-13} and 9.3×10^{-13} cm^2 s^{-1}, respectively. These values are comparable to the Li-ion diffusion coefficient (D_{Li^+}) in conventional LIB cathode materials, such as $LiCoO_2$ (10^{-13}–10^{-11} cm^2 s^{-1})[48] and $LiFePO_4$ (10^{-16}–10^{-14} cm^2 s^{-1}).[49] In addition, GITT measurements of ncNTP were conducted to calculate the Na-ion diffusion coefficient (D_{Na^+}). The average D_{Na^+} values during discharge and charge in the plateau region (SOC 20–80%) were 5.4×10^{-13} and 2.8×10^{-12} cm^2 s^{-1}, respectively (Fig. S13†). The obtained $D_{Ca^{2+}}$ is lower than D_{Na^+}, suggesting that Ca^{2+} diffusion in NTP is slower than Na^+ diffusion, which may explain the performance discrepancy between the Ca full-cells and Na half-cells.

Mechanism of Ca storage in NTP

The mechanism of Ca storage in NTP was investigated using *ex situ* FE-SEM, EDS, XRD, and XPS. Analyses were performed on the ncNTP electrode in three states: pristine, fully discharged (1.5 V), and fully charged (2.6 V). To ensure the removal of the Ca electrolyte salts from the surface, the ncNTP electrodes were thoroughly washed with a mixed solvent of DME and THF.

The FE-SEM images confirmed that the embedded NTP nanoparticles did not undergo significant morphological changes (Fig. S14†). The morphology of the NTP nanoparticles after both discharging and charging remained similar to that of their as-deposited state, indicating that no significant damage or deformation of NTP particles occurred during the discharging and charging processes. To quantify the amount of Ca^{2+} inserted and extracted within the NTP, EDS analysis was performed (Fig. S15†). The EDS spectra were normalised to the Ti signal. After discharge, Ca signals were observed at 3.7 keV (Ca Kα) and 4.0 keV (Ca Kβ). After charging, the intensity of the Ca signal was reduced compared to that in the discharge state, indicating the extraction of Ca^{2+} from the NTP framework. The amount of Ca quantified by EDS agreed well with calculated values from electrochemical studies. Additionally, the Na content remained relatively constant after both discharging and charging, suggesting that the reaction predominantly involved Ca^{2+} transport.

Ex situ XRD analysis was conducted after discharging and charging to investigate the structural changes during the insertion and extraction of Ca^{2+} within the NTP framework (Fig. 3a). In the pristine state, peaks corresponding to NTP were observed, along with a broad peak at approximately 18°, attributed to the CNT and dome of the sample holder, and a peak at approximately 43°, originating from the sample holder. After discharge, the peak intensity of NTP was reduced, and peaks corresponding to new phases appeared at 23.7°, 28.6°, 32.1°, and 35.2°. For Na^+ insertion into NTP, the main

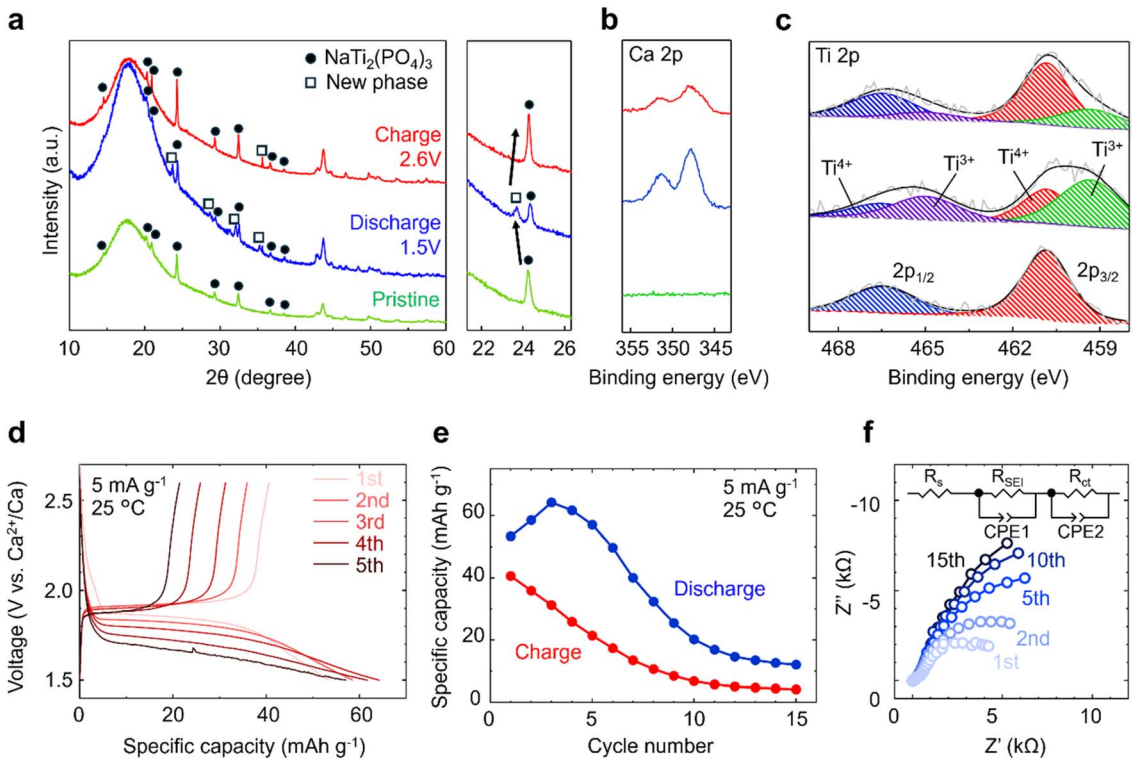

Fig. 3 Analysis of the Ca storage mechanism in NTP. (a) *Ex situ* XRD profiles of the ncNTP cathode before and after the 1st cycle. (b) Ca 2p and (c) Ti 2p XPS profiles of the ncNTP cathode before and after the 1st cycle. (d) Voltage profiles of ncNTP for a rate of 5 mA g^{-1} at 25 °C during the 1st to 5th cycles. (e) Cycling performance of ncNTP during the 1st to 15th cycles. (f) Nyquist plots of ncNTP measured after discharge for each cycle.

peak corresponding to the (113) plane at 24.2° disappeared, and a new peak associated with the (113) plane of $Na_3Ti_2(PO_4)_3$ appeared at 23.5°.[44] In this study, a similar phenomenon was observed for Ca^{2+} insertion into NTP: the peak corresponding to the (113) plane at 24.3° disappeared, and a new peak emerged at 23.7°. This suggests that $Ca_xNaTi_2(PO_4)_3$ (CaNTP), which is formed by the insertion of Ca^{2+} into NTP, has a crystal structure similar to that of $Na_3Ti_2(PO_4)_3$. In addition, the (024) and (116) planes of $Na_3Ti_2(PO_4)_3$ at 28.5° and 31.8°, respectively, were similar to the new peaks of CaNTP at 28.6° and 32.1°, which is consistent with the above discussion. Furthermore, for Ca^{2+} insertion into $NaV_2(PO_4)_3$, which has the same crystal structure as NTP, it has been reported that the peak shifts during Na^+ and Ca^{2+} insertion are similar, supporting the above interpretation.[50–52] The peak at 35.2° is attributed to the formation of $CaCO_3$ as part of the cathode–electrolyte interphase (CEI) on the electrode surface. Residual peaks of NTP were also observed, indicating the presence of unreacted NTP, possibly owing to the large number of NTP particles. After charging, the peaks corresponding to the new phase disappeared, and the intensities of the NTP peaks increased, suggesting the successful extraction of Ca^{2+} from NTP.

To investigate the insertion and extraction of Ca^{2+} within NTP, as well as the changes in the oxidation state of Ti during discharging and charging, XPS analyses were conducted (Fig. 3b and c). For the pristine electrode, no Ca 2p peak was observed, and the Ti 2p spectrum showed the presence of only Ti^{4+}. Upon discharging to 1.5 V, Ca 2p peaks appeared at 347.8 and 351.4 eV, indicating the presence of Ca on the electrode after discharge. Additionally, the Ti 2p spectrum shifted to a lower binding energy, exhibiting two peaks corresponding to Ti^{4+} and Ti^{3+}, which suggested that the Ti in NTP was partially reduced by Ca insertion. After charging, the intensity of the Ca 2p peaks was reduced, indicating the extraction of Ca^{2+} from NTP. However, residual Ca 2p peaks remained, indicating the presence of partially unreacted NTP or the formation of a CEI layer containing $Ca(CB_{11}H_{12})_2$ salts. According to the changes in the valence state of Ti in NTP calculated through the deconvolution of the XPS profiles, the reaction can be formulated as follows.

$$\text{Discharge: } NaTi_2(PO_4)_3 + 0.62Ca^{2+} + 1.24e^- \rightarrow 0.62CaNaTi_2(PO_4)_3 + 0.38NaTi_2(PO_4)_3$$

$$\text{Charge: } 0.62CaNaTi_2(PO_4)_3 + 0.38NaTi_2(PO_4)_3 \rightarrow 0.26CaNaTi_2(PO_4)_3 + 0.74NaTi_2(PO_4)_3 + 0.36Ca^{2+} + 0.72e^-$$

To further investigate the CEI, additional XPS analyses were performed on C and O before and after charging (Fig. S16†). The C 1s peak remained unchanged, indicating that the CNT and binder in the electrode were chemically stable and did not degrade. The deconvoluted O 1s peak revealed contributions from P=O, O from PO_4 units in the NTP lattice, C=O, and COO groups, as well as O from the CNT and binder, including adsorbed O and surface oxides. The P=O component did not change during the discharge and charge cycles, demonstrating the high stability of the NTP structure. In contrast, the C=O component decreased during discharging and charging, suggesting the reduction of surface oxides on the CNT and the binder and/or adsorbed oxygen. The C–O–C component increased during discharging and charging, implying the formation and accumulation of a polymeric CEI derived from the ether-based solvents, *i.e.* DME and THF.

The voltage profiles from the 1st to 5th cycles are shown in Fig. 3d. Reversible charging and discharging were observed in each cycle. An increase in the overvoltage was noted during discharge. It has been proposed that the highly Ca-rich NVP becomes electrochemically inert. It is likely that the increase in overvoltage is related to the accumulation of electrochemically inert, highly Ca-rich NTP over successive cycles. The cycling performance of NTP is shown in Fig. 3e. A gradual increase in the discharge capacity was observed during the 1st to 3rd cycles, which was not observed for the Na half-cell (Fig. S8†). These results suggest that electrolyte decomposition and CEI-layer growth contribute to the observed behaviour. Beyond the 3rd cycle, capacity degradation was observed during the discharge and charge cycles.

To investigate the degradation mechanisms during charge–discharge cycling, EIS measurements were performed after each cycle, and the results were analysed using an equivalent circuit model. The Nyquist plots obtained after discharge for different cycles (Fig. 3f and S17a†) exhibited characteristic features, including a high-frequency semicircle and mid-frequency semicircle, which correspond to electrolyte resistance (R_s), solid electrolyte interphase (SEI) resistance (R_{SEI}), and charge transfer resistance (R_{ct}), respectively. In the initial cycle, the EIS spectrum showed a relatively small R_{ct}, indicating efficient transfer at the electrode–electrolyte interface. However, with increasing cycle number, R_{ct} exhibited a progressive increase, suggesting a deterioration in interfacial charge transfer kinetics. This degradation is likely caused by structural distortions or the loss of active sites for Ca^{2+} intercalation/extraction, which may result from the accumulation of residual Ca^{2+} in NTP. In contrast, during charging, no significant increase in the R_{ct} was observed after the 2nd cycle (Fig. S17b†), indicating that the degradation mechanism is mainly associated with the discharge process (Ca^{2+} insertion) rather than the charge process. These findings highlight the importance of optimizing the discharge process to improve long-term cycling performance.

Conclusions

In this study, the electrochemical properties of ncNTP as a Ca^{2+} host material were investigated using a Ca full-cell with the hydride-based electrolyte $Ca(CB_{11}H_{12})_2$ in DME/THF. NTP nanoparticles, 10–50 nm in size, were synthesised *via* a solvothermal method and were highly dispersed and entangled within the CNT network. The Ca-metal battery using ncNTP exhibited smaller voltage hysteresis and flatter plateaus than previously reported cathodes for Ca-metal batteries. The reversible insertion/extraction of Ca^{2+} was confirmed by *ex situ* XRD, XPS, and SEM analyses. However, unreacted NTP and residual Ca^{2+} were also observed, which appeared to contribute

to the poor cycling performance. To facilitate these reactions, it is necessary to enhance Ca^{2+} diffusivity in the cathode and reduce the desolvation energy of the electrolyte. This study highlights the potential and challenges of developing practical oxide cathodes for Ca-metal batteries with rapid Ca^{2+} diffusion.

Data availability

All relevant experimental data within the article will be provided by the corresponding author on reasonable request.

Author contributions

K. K. conceived and designed the study. K. S. performed the synthesis, measurements, and data analysis. K. I. and H. Y. performed SEM and TEM observations. K. K., T. S., and S. O. discussed the results. K. S. wrote the manuscript. K. K. and S. O. supervised the study. All authors discussed and commented on the manuscript.

Conflicts of interest

There are no conflicts to declare.

Acknowledgements

This work was supported by the JSPS KAKENHI Grant-in-Aid for Scientific Research B (No. 22H01803), Scientific Research A (No. 23H00301), and JST FOREST Program (Grant Number JPMJFR236F). It was also supported by Sumitomo Metal Mining Co., Ltd. Additional support was provided by Amano Institute of Technology, the Murata Science and Education Foundation (No. M24AN132), and the Iketani Science and Technology Foundation (No. 0361179-A). We thank H. Ohmiya and N. Warifune of Tohoku University for their technical assistance.

Notes and references

1 C. Xu, P. Behrens, P. Gasper, K. Smith, M. Hu, A. Tukker and B. Steubing, *Nat. Commun.*, 2023, **14**, 119.
2 F. Aguilar Lopez, D. Lauinger, F. Vuille and D. B. Muller, *Nat. Commun.*, 2024, **15**, 4179.
3 X. Wang, G. Tan, Y. Bai, F. Wu and C. Wu, *Electrochem. Energy Rev.*, 2020, **4**, 35–66.
4 C. Chen, F. Shi and Z. Xu, *J. Mater. Chem. A*, 2021, **9**, 11908–11930.
5 J. Muldoon, C. B. Bucur and T. Gregory, *Chem. Rev.*, 2014, **114**, 11683–11720.
6 A. M. Melemed, A. Khurram and B. M. Gallant, *Batteries Supercaps*, 2020, **3**, 570–580.
7 R. J. Gummow, G. Vamvounis, M. B. Kannan and Y. He, *Adv. Mater.*, 2018, **30**, e1801702.
8 D. Aurbach, G. S. Suresh, E. Levi, A. Mitelman, O. Mizrahi, O. Chusid and M. Brunelli, *Adv. Mater.*, 2007, **19**, 4260–4267.
9 L. F. Wan, B. R. Perdue, C. A. Apblett and D. Prendergast, *Chem. Mater.*, 2015, **27**, 5932–5940.
10 G. Gupta, R. Gupta, A. Gupta and D. Kumar, *J. Phys. D: Appl. Phys.*, 2024, **57**, 485503.
11 A. L. Lipson, S. Kim, B. Pan, C. Liao, T. T. Fister and B. J. Ingram, *J. Power Sources*, 2017, **369**, 133–137.
12 J. Wang, S. Tan, F. Xiong, R. Yu, P. Wu, L. Cui and Q. An, *Chem. Commun.*, 2020, **56**, 3805–3808.
13 S. J. R. Prabakar, W. Park, J. Y. Seo, S. P. Singh, D. Ahn, K. Sohn and M. Pyo, *Energy Storage Mater.*, 2021, **43**, 85–96.
14 X. Xu, M. Duan, Y. Yue, Q. Li, X. Zhang, L. Wu, P. Wu, B. Song and L. Mai, *ACS Energy Lett.*, 2019, **4**, 1328–1335.
15 P. Padigi, G. Goncher, D. Evans and R. Solanki, *J. Power Sources*, 2015, **273**, 460–464.
16 T. N. Vo, H. Kim, J. Hur, W. Choi and T. Kim, *J. Mater. Chem. A*, 2018, **6**, 22645–22654.
17 J. Wang, Y. Zhang, F. Qiao, Y. Jiang, R. Yu, J. Li, S. Lee, Y. Dai, F. Guo, P. Jiang, L. Zhang, Q. An, G. He and L. Mai, *Adv. Mater.*, 2024, **36**, e2403371.
18 J. Wang, J. Wang, Y. Jiang, F. Xiong, S. Tan, F. Qiao, J. Chen, Q. An and L. Mai, *Adv. Funct. Mater.*, 2022, **32**, 2113030.
19 Z. L. Xu, J. Park, J. Wang, H. Moon, G. Yoon, J. Lim, Y. J. Ko, S. P. Cho, S. Y. Lee and K. Kang, *Nat. Commun.*, 2021, **12**, 3369.
20 C. Chen, F. Shi, S. Zhang, Y. Su and Z. L. Xu, *Small*, 2022, **18**, e2107853.
21 D. Wang, X. Gao, Y. Chen, L. Jin, C. Kuss and P. G. Bruce, *Nat. Mater.*, 2018, **17**, 16–20.
22 T. Shinohara, K. Kisu, A. Dorai, K. Zushida, H. Yabu, S. Takagi and S. Orimo, *Adv. Sci.*, 2024, **11**, e2308318.
23 Z. Li, O. Fuhr, M. Fichtner and Z. Zhao-Karger, *Energy Environ. Sci.*, 2019, **12**, 3496–3501.
24 A. Shyamsunder, E. Blanc, A. Assoud and F. Nazar, *ACS Energy Lett.*, 2019, **4**, 2271–2276.
25 K. Kisu, S. Kim, T. Shinohara, K. Zhao, A. Zuttel and S. Orimo, *Sci. Rep.*, 2021, **11**, 7563.
26 K. Kisu, A. Dorai, K. Hatakeyama-Sato, T. Takano, S. Takagi, K. Oyaizu and S. Orimo, *ACS Appl. Mater. Interfaces*, 2025, **17**, 1322–1331.
27 Z. Li, B. P. Vinayan, T. Diemant, R. J. Behm, M. Fichtner and Z. Zhao-Karger, *Small*, 2020, **16**, e2001806.
28 A. Scafuri, R. Berthelot, K. Pirnat, A. Vizintin, J. Bitenc, G. Aquilanti, D. Foix, R. Dedryvère, I. Arčon, R. Dominko and L. Stievano, *Chem. Mater.*, 2020, **32**, 8266–8275.
29 N. J. Leon, X. Xie, M. Yang, D. M. Driscoll, J. G. Connell, S. Kim, T. Seguin, J. T. Vaughey, M. Balasubramanian, K. A. Persson and C. Liao, *J. Phys. Chem. C*, 2022, **126**, 13579–13584.
30 K. Kisu, R. Mohtadi and S. Orimo, *Adv. Sci.*, 2023, **10**, e2301178.
31 Z. Li, B. P. Vinayan, P. Jankowski, C. Njel, A. Roy, T. Vegge, J. Maibach, J. M. G. Lastra, M. Fichtner and Z. Zhao-Karger, *Angew. Chem., Int. Ed.*, 2020, **59**, 11483–11490.
32 S. Kim, N. T. Hahn, T. T. Fister, N. J. Leon, X. Lin, H. Park, P. Zapol, S. H. Lapidus, C. Liao and J. T. Vaughey, *Chem. Mater.*, 2023, **35**, 2363–2370.
33 J. Park, Z. L. Xu, G. Yoon, S. K. Park, J. Wang, H. Hyun, H. Park, J. Lim, Y. J. Ko, Y. S. Yun and K. Kang, *Adv. Mater.*, 2020, **32**, e1904411.

34 H. Song, Y. Li, F. Tian and C. Wang, *Adv. Funct. Mater.*, 2022, **32**, 2200004.
35 Z. Zhao-Karger, Y. Xiu, Z. Li, A. Reupert, T. Smok and M. Fichtner, *Nat. Commun.*, 2022, **13**, 3849.
36 J. Bitenc, A. Scafuri, K. Pirnat, M. Lozinšek, I. Jerman, J. Grdadolnik, B. Fraisse, R. Berthelot, L. Stievano and R. Dominko, *Batteries Supercaps*, 2020, **4**, 214–220.
37 Y. Xiu, A. Mauri, S. Dinda, Y. Pramudya, Z. Ding, T. Diemant, A. Sarkar, L. Wang, Z. Li, W. Wenzel, M. Fichtner and Z. Zhao-Karger, *Angew. Chem., Int. Ed.*, 2023, **62**, e202212339.
38 O. Lužanin, A. K. Lautar, T. Pavčnik and J. Bitenc, *Mater. Adv.*, 2024, **5**, 642–651.
39 R. Li, Y. Lee, H. Lin, X. Che, X. Pu, Y. Yi, F. Chen, J. Yu, C. Chan, K. Park and Z. Xu, *Adv. Energy Mater.*, 2024, **14**, 2302700.
40 T. Koketsu, J. Ma, B. J. Morgan, M. Body, C. Legein, W. Dachraoui, M. Giannini, A. Demortiere, M. Salanne, F. Dardoize, H. Groult, O. J. Borkiewicz, K. W. Chapman, P. Strasser and D. Dambournet, *Nat. Mater.*, 2017, **16**, 1142–1148.
41 M. Kim, J. Park, H. Kim, J. Lee, I. Lee, J. Kim, S. Lee and K. Min, *Energy Storage Mater.*, 2024, **73**, 103827.
42 H. Zhang, B. Qin, D. Buchholz and S. Passerini, *ACS Appl. Energy Mater.*, 2018, **1**, 6425–6432.
43 D. Wang, Q. Liu, C. Chen, M. Li, X. Meng, X. Bie, Y. Wei, Y. Huang, F. Du, C. Wang and G. Chen, *ACS Appl. Mater. Interfaces*, 2016, **8**, 2238–2246.
44 C. Xu, Y. Xu, C. Tang, Q. Wei, J. Meng, L. Huang, L. Zhou, G. Zhang, L. He and L. Mai, *Nano Energy*, 2016, **28**, 224–231.
45 M. Wu, W. Ni, J. Hu and J. Ma, *Nanomicro Lett.*, 2019, **11**, 44.
46 T. Shinohara, K. Kisu, S. Takagi and S. Orimo, *Energy Adv.*, 2024, **3**, 2758–2763.
47 D. B. Tekliye, A. Kumar, X. Weihang, T. D. Mercy, P. Canepa and G. Sai Gautam, *Chem. Mater.*, 2022, **34**, 10133–10143.
48 H. Xia, L. Lu and G. Ceder, *J. Power Sources*, 2006, **159**, 1422–1427.
49 P. Prosini, *Solid State Ionics*, 2002, **148**, 45–51.
50 B. Jeon, J. W. Heo, J. Hyoung, H. H. Kwak, D. M. Lee and S. Hong, *Chem. Mater.*, 2020, **32**, 8772–8780.
51 S. Kim, L. Yin, M. Lee, P. Parajuli, L. Blanc, T. Fister, H. Park, B. Kwon, B. Ingram, P. Zapol, R. Klie, K. Kang, F. Nazar, H. Lapidus and T. Vaughey, *ACS Energy Lett.*, 2020, **5**, 3203–3211.
52 L. E. Blanc, Y. Choi, A. Shyamsunder, B. Key, S. H. Lapidus, C. Li, L. Yin, X. Li, B. Gwalani, Y. Xiao, C. J. Bartel, G. Ceder and L. F. Nazar, *Chem. Mater.*, 2022, **35**, 468–481.